Available online at www.sciencedirect.com
SCIENCE DIRECT®
Journal of Computational Physics 213 (2006) 730–747
JOURNAL OF COMPUTATIONAL PHYSICS
www.elsevier.com/locate/jcp

Fourier spectral simulations and Gegenbauer reconstructions for electromagnetic waves in the presence of a metal nanoparticle

Mi-Sun Min [a,*], Tae-Woo Lee [b], Paul F. Fischer [a], Stephen K. Gray [b]

[a] *Mathematics and Computer Science Division, Argonne National Laboratory, 9700 S. Cass Avenue, Argonne, IL 60439, USA*
[b] *Chemistry Division, Argonne National Laboratory, 9700 S. Cass Avenue, Argonne, IL 60439, USA*

Received 2 December 2004; received in revised form 17 May 2005; accepted 20 June 2005
Available online 20 October 2005

Abstract

We describe Fourier pseudospectral time-domain simulations, carried out in order to study light interacting with a metallic nanoscale object. The difficulty of using Fourier methods to accurately predict the electromagnetic scattering in such problems arises from the discontinuity in the dielectric function along the surface of the metallic object. Standard Fourier methods lead to oscillatory behavior in approximating solutions that are nonsmooth or that have steep gradients. By applying the Gegenbauer reconstruction technique as a postprocessing method to the Fourier pseudospectral solution, we successfully reduce the oscillations after postprocessing.

Our computational results, including comparison with finite-difference time-domain simulations, demonstrate the efficiency and accuracy of the method.

Keywords: Fourier pseudospectral method; Gegenbauer reconstruction; Postprocessing

1. Introduction

Metallic nanostructures, such as metal nanoparticles and nanoholes in thin metal films, are of considerable interest because of the possibility of creating surface plasmon excitations when interacting with light [2,23]. Surface plasmons are collective electronic excitations that effectively concentrate and confine light energy [4]. The manipulation of surface plasmons could lead to novel nanoscale optoelectronic devices.

Numerical simulations help us to understand and predict the basic physics of such nanophotonics problems and also provide cost-effective tools for prototyping design of potential devices. Among general computational techniques employed in such simulations, Fourier methods have been naturally considered for problems with periodic features, such as planar waveguides and photonic crystal structures for integrated photonic devices. Computational implementations and their error estimates have been analyzed in the literature [9,26]. In this

* Corresponding author.
E-mail addresses: mmin@mcs.anl.gov (M.-S. Min), twlee@tcg.anl.gov (T.-W. Lee), fischer@mcs.anl.gov (P.F. Fischer), gray@tcg.anl.gov (S.K. Gray).

0021-9991/$ - see front matter
doi:10.1016/j.jcp.2005.06.025

paper, we show how such Fourier methods can be applied to light interacting with metal nanostructures that do not possess periodic features. Our focus is on mathematical reconstruction techniques for Fourier pseudospectral simulation data for which one might consider Fourier–Padé or Gegenbauer approximations [6,16,24,26,27].

As a first step, we study light interacting with a small metallic cylinder or nanowire of diameter of 50 nm and infinite length in a vacuum. Before presenting detailed mathematical formulae, we give a brief overview of the mechanism behind surface plasmon excitation in such a system. Imagine the circular cross-section of the nanowire to be in the x–y plane with its long axis parallel to the z-axis. Incident light traveling along the x-axis with y-polarization is then capable of inducing dipolar (and higher-order) charge oscillations near the metal surfaces. These charge oscillations are associated with collective excitations of electrons near the metal surfaces and can lead to electromagnetic surface waves that are highly localized (evanescent) near surfaces, namely, surface plasmons. A complex-valued dielectric constant is used to describe the metallic response to radiation. More detailed analysis shows that this dielectric constant must have a negative real part for surface plasmons to be reasonably excited. Absorption of radiation by the metal can also occur, which involves introducing an imaginary part to the dielectric constant. In addition to being highly localized, the field intensities of surface plasmon excitations can be extremely large near the metal surfaces.

Many approaches exist for solving the relevant Maxwell's wave equations. In this paper we are concerned with time-domain methods that involve grids in space and time. The advantages of such methods include conceptual simplicity and the ability to model a variety of complex system architectures. The most popular time-domain approach is the finite-difference time-domain (FDTD) method [31,30]. It involves low-order finite differencing to accomplish both spatial and time derivatives. In order to describe surface plasmon behavior accurately, however, very fine grids in both space and time are required. An alternative to FDTD that can lead to better accuracy with larger grid spacings would be to evaluate the spatial derivatives with Fourier methods. Such pseudospectral time-domain (PSTD) methods have been proposed and studied in the context of nonplasmonic systems [21,27]. However the abrupt, sharp changes in magnitudes of the electromagnetic fields near the metal surfaces as a result of surface plasmons is problematic for PSTD methods. In particular, nonphysical oscillations, called Gibbs oscillations, can occur that contaminate the solution over a wide range of coordinate space. However, the finite Fourier data contains enough information about the original solution that one can reexpress the data as a Padé or Gegenbauer finite expansion and can thus reduce the oscillations. In both cases, the reconstructions require obtaining the coefficients for the reconstructed approximations in terms of the Fourier coefficients. Implementations with Fourier–Padé reconstructions in [26] have successfully reduced the oscillations for Fourier pseudospectral solutions of nonlinear partial differential equations such as Burgers' and Boussinesq equations.

Here, we apply the Gegenbauer reconstruction to Fourier pseudospectral time-domain simulations [21] of Maxwell's equations. The computational results show that the Gegenbauer reconstructions successfully reduce the noise in the Fourier pseudospectral simulations.

This paper is organized as follows. Section 2 gives the formulation of Maxwell's equations and the auxiliary differential equation [18,30] for the current term from the Drude model. Section 3 presents our numerical discretizations in space and time and the setup of parameters for PSTD simulations. Section 4 introduces cost-effective Gegenbauer reconstructions in one and two dimensions as postprocessing methods for PSTD solutions. Their convergence behaviors are demonstrated for some piecewise analytic functions in one dimension. CPU times for simulations are also discussed. Section 5 demonstrates the PSTD solutions from the nanoparticle scattering simulations and their postprocessed results. FDTD results computed on very finer grids are also provided for comparison with reconstructed results. Section 6 discusses the remaining issues concerning computational automation, with an appropriate error estimate for reconstructed solutions varying with free parameters. Section 7 briefly summarizes our research.

2. Maxwell's equations for metal nanoparticles

We consider the electrodynamics of metal nanosystems, such as those in [2,4,18,19,23], which are composed of (nonmagnetic) metals and dielectric materials. The frequency-domain Maxwell's equations for the electric and magnetic field vectors, $\tilde{E}$ and $\tilde{H}$, may then be taken to be [4]:

$$-\mathrm{i}\omega\tilde{\epsilon}\tilde{E} = \nabla \times \tilde{H}, \tag{1}$$

$$\mathrm{i}\omega\mu_0\tilde{H} = \nabla \times \tilde{E}, \tag{2}$$

where ω is the temporal frequency and μ_0 is the magnetic permeability. Each specific system is defined by the spatial and frequency dependence of the dielectric constant $\tilde{\epsilon}$. Dielectric regions of space can often be described by a positive, real, and frequency-independent dielectric constant. Metallic regions involve a generally complex-valued frequency-dependent dielectric constant. Moreover, the real part of the metallic dielectric constant can be negative, an essential feature for surface plasmon behavior. This latter property can lead to instability in naive time-domain formulations of Eq. (1).

To address the difficulties noted above, we implement a Drude model [4] of the metallic dielectric constant within an auxiliary differential equation approach [30], as outlined in more detail in [18]. For metallic regions, we first reexpress $\tilde{\epsilon} = \epsilon_0\epsilon_\mathrm{p}$ as

$$\tilde{\epsilon} = \epsilon_0[\epsilon_\infty + (\epsilon_\mathrm{p} - \epsilon_\infty)], \tag{3}$$

where ϵ_0 is the permittivity of free space, ϵ_∞ is the infinite frequency value for the dielectric constant, and ϵ_p will be specified later. Identifying the current density as

$$\tilde{J} = -\mathrm{i}\omega\epsilon_0(\epsilon_\mathrm{p} - \epsilon_\infty)\tilde{E}, \tag{4}$$

we rewrite Eq. (1) as

$$\tilde{J} - \mathrm{i}\omega\epsilon_0\epsilon_\infty\tilde{E} = \nabla \times \tilde{H}. \tag{5}$$

Inverse Fourier transforming (5) gives

$$J(t) + \epsilon_0\epsilon_\infty\frac{\partial E(t)}{\partial t} = \nabla \times H(t). \tag{6}$$

The following is the Drude model [4,18,30] for the optical properties of a free-electron metal:

$$\epsilon_\mathrm{p} = \epsilon_\infty - \frac{\omega_\mathrm{p}^2}{\omega^2 + \mathrm{i}\Gamma_\mathrm{p}\omega}, \tag{7}$$

where Γ_p is the Drude damping coefficient and ω_p is the plasmon frequency. This leads to

$$\frac{\partial^2 J(t)}{\partial t^2} + \Gamma_\mathrm{p}\frac{\partial J(t)}{\partial t} = \epsilon_0\omega_\mathrm{p}^2\frac{\partial E(t)}{\partial t}. \tag{8}$$

Reducing the order of the ordinary differential equation, we have

$$\frac{\partial J(t)}{\partial t} + \Gamma_\mathrm{p}J(t) = \epsilon_0\omega_\mathrm{p}^2E(t). \tag{9}$$

Equipped with Eq. (9) for the current term, we define the governing time-domain equations as:

$$\epsilon\frac{\partial E}{\partial t} = \nabla \times H - J, \tag{10}$$

$$\mu\frac{\partial H}{\partial t} = -\nabla \times E, \tag{11}$$

$$\frac{\partial J}{\partial t} = \alpha J + \beta E, \tag{12}$$

where the phenomenological parameters in free space are:

$$\epsilon = \epsilon_0, \quad \mu = \mu_0, \quad \alpha = 0, \quad \text{and} \quad \beta = 0 \tag{13}$$

and in the metallic region are:

$$\epsilon = \epsilon_0\epsilon_\infty, \quad \mu = \mu_0, \quad \alpha = -\Gamma_\mathrm{p}, \quad \text{and} \quad \beta = \epsilon_0\omega_\mathrm{p}^2. \tag{14}$$

The values for the coefficients ϵ_∞, Γ_p, and ω_p can be obtained from fits of experimental dielectric information [18].

The electromagnetic field vectors and the current vector are generally written by decomposing each component as follows:

$$E = (E_x, E_y, E_z), \quad H = (H_x, H_y, H_z), \quad J = (J_x, J_y, J_z). \tag{15}$$

Here, we consider the transverse-electric mode in two dimensions:

$$E = (E_x, E_y, 0), \quad H = (0, 0, H_z), \quad \text{and} \quad J = (J_x, J_y, 0). \tag{16}$$

Then the governing equations (10) and (11) are written as

$$\frac{\partial F}{\partial t} = A\frac{\partial F}{\partial x} + B\frac{\partial F}{\partial y} + CF, \tag{17}$$

where the field vector is $F = [E_x, E_y, H_z, J_x, J_y]^{\mathrm{T}}$ and the coefficient matrices are:

$$A = \begin{bmatrix} 0 & 0 & 0 & 0 & 0 \\ 0 & 0 & -\frac{1}{\epsilon} & 0 & 0 \\ 0 & -\frac{1}{\mu} & 0 & 0 & 0 \\ 0 & 0 & 0 & 0 & 0 \\ 0 & 0 & 0 & 0 & 0 \end{bmatrix}, \quad B = \begin{bmatrix} 0 & 0 & \frac{1}{\epsilon} & 0 & 0 \\ 0 & 0 & 0 & 0 & 0 \\ \frac{1}{\mu} & 0 & 0 & 0 & 0 \\ 0 & 0 & 0 & 0 & 0 \\ 0 & 0 & 0 & 0 & 0 \end{bmatrix}, \quad \text{and} \quad C = \begin{bmatrix} 0 & 0 & 0 & 0 & 0 \\ 0 & 0 & 0 & 0 & 0 \\ 0 & 0 & 0 & 0 & 0 \\ \beta_x & 0 & 0 & \alpha_x & 0 \\ 0 & \beta_y & 0 & 0 & \alpha_y \end{bmatrix}.$$

One can check the well-posedness of this formulation. Eq. (12) contains no spatial derivatives, and hence it is indeed an ODE for J. After the undifferentiated terms in Eq. (17) are dropped, it becomes a 3×3 Maxwell system. One can symmetrize it through the following change of variables [17]:

$$G = (E_x, E_y, \sqrt{\mu/\epsilon}H_z). \tag{18}$$

Thus, the system is symmetric hyperbolic and therefore strongly well-posed [8].

3. Numerical scheme

Let us define the computational domain on $[0,L_x] \times [0,L_y]$, where $L_x = 1024$ nm and $L_y = 512$ nm. The grid points are defined by

$$x_i = \frac{L_x i}{N_x} \ (i = 0, \ldots, N_x - 1) \quad \text{and} \quad y_j = \frac{L_y j}{N_y} \ (j = 0, \ldots, N_y - 1). \tag{19}$$

Consider a metal cylinder with radius 25 nm whose center is placed at $x = 767.5$ nm and $y = 255.5$ nm in the computational domain (see Fig. 1). The parameters of the equations in (14) for the metallic region are chosen as $\epsilon_\infty = 8.926$, $\Gamma_{\mathrm{p}} = -3.08 \times 10^{14}$ Hz, and $\omega_{\mathrm{p}} = 1.7577 \times 10^{16}$ Hz, as in [18,19]. Since we simulate infinite-space solutions on a finite computational domain, we introduce an artificial absorbing layer in order to absorb field components that approach the boundaries. The thickness of the absorbing layer is set to 28 and 40 nm in the x- and y-direction, respectively. We use the uniaxial perfectly matched layer (UPML) formulation [28,30]; in this region the field intensity vanishes as it reaches to the boundary of the computational domain. Thus, it is reasonable to consider this problem as a periodic problem and to apply Fourier approximations globally in the computational domain.

The pseudospectral time-domain (PSTD) scheme [13,14] we use involves second-order explicit leap-frogging in time, just as ordinary FDTD, but replaces the spatial derivatives by the Fourier pseudospectral differentiation operators, denoted by D_x and D_y below. At the time level $t^n = n\Delta t$, our scheme is written as follows:

$$\bar{\epsilon}\frac{\bar{E}_x^{n+\frac{1}{2}} - \bar{E}_x^{n-\frac{1}{2}}}{\Delta t} = D_y \bar{H}_z^n - \bar{J}_x^n, \tag{20}$$

$$\bar{\epsilon}\frac{\bar{E}_y^{n+\frac{1}{2}} - \bar{E}_y^{n-\frac{1}{2}}}{\Delta t} = -D_x \bar{H}_z^n + \bar{J}_y^n, \tag{21}$$

$$\bar{\mu}\frac{\bar{H}_z^{n+1} - \bar{H}_z^n}{\Delta t} = D_y \bar{E}_x^{n+\frac{1}{2}} - D_x \bar{E}_y^{n+\frac{1}{2}}, \tag{22}$$

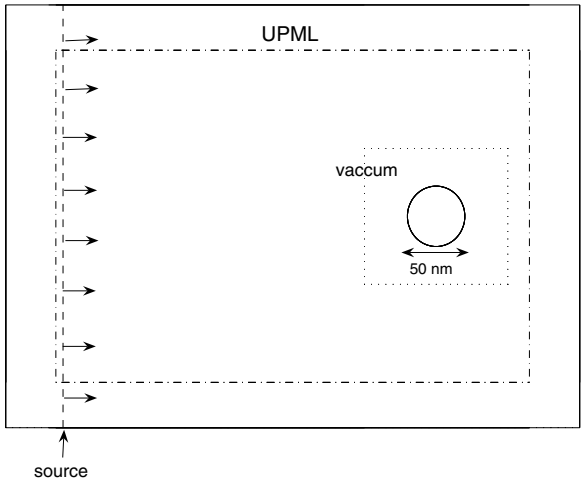

Fig. 1. Schematic depiction of the computational domain on $[0,1024]\times[0,512]\,\mathrm{nm}^2$.

$$\frac{\bar{J}_x^{n+1}-\bar{J}_x^n}{\Delta t}=\bar{\alpha}\frac{\bar{J}_x^{n+1}+\bar{J}_x^n}{2}+\bar{\beta}\bar{E}_x^{n+1/2}, \tag{23}$$

$$\frac{\bar{J}_y^{n+1}-\bar{J}_y^n}{\Delta t}=\bar{\alpha}\frac{\bar{J}_y^{n+1}+\bar{J}_y^n}{2}+\bar{\beta}\bar{E}_y^{n+1/2}, \tag{24}$$

where the vector representations of the fields and parameters are defined, respectively, by:

$$\bar{E}_x^n=[(E_x)_{00},(E_x)_{10},\ldots,(E_x)_{ij},\ldots,(E_x)_{N_x-1N_y-1}]^{\mathrm{T}}\quad\text{for}\quad(E_x)_{ij}=E_x(x_i,y_j), \tag{25}$$

$$\bar{\epsilon}=\bar{\epsilon}_{ij}=\epsilon(x_i,y_j),\quad\bar{\alpha}=\bar{\alpha}_{ij}=\alpha(x_i,y_j)\quad\text{and}\quad\bar{\beta}=\bar{\beta}_{ij}=\beta(x_i,y_j) \tag{26}$$

and the spatial derivatives represent $D_x=I\otimes\hat{D}_x$ and $D_y=\hat{D}_y\otimes I$ using the tensor product $\otimes$ defined in [5], where $\hat{D}_x$ and $\hat{D}_y$ are the one-dimensional differentiation matrices of sizes $N_x\times N_x$ and $N_y\times N_y$, respectively, whose components are defined in physical space as in [13]. Of course, in practice, fast Fourier transforms are used to effectively evaluate the action of these matrices on vectors. Note that a common, evenly spaced non-staggered spatial grid is assumed for all field variables, which is simpler than the FDTD/Yee [31] gridding scheme.

In our problem configuration, the solution is piecewise smooth as a result of the discontinuity in the dielectric function along the interface of the cylinder. Hence, we cannot obtain an accurate approximate solution with the standard Fourier pseudospectral method (20)–(24), although that is a good method for analytic and periodic functions. The numerical solutions obtained by the standard Fourier pseudospectral time-domain simulations are obscured by oscillations arising from the Gibbs phenomenon. However, one can recover accurate solutions by postprocessing techniques such as Fourier–Padé [6,27] and Gegenbauer postprocessing [16,24]. In the following section, we introduce a cost-effective Gegenbauer reconstruction technique as a postprocessing method and use it to increase the order of accuracy for our PSTD solutions by resolving the nonphysical oscillations.

4. Gegenbauer postprocessing

Gegenbauer reconstruction [13] requires a priori knowledge of the location of the discontinuity. In the present application, the discontinuity location, which arises from the jump in dielectric function, is specified as part of the problem definition, and Gegenbauer reconstruction is therefore appropriate.

We briefly revisit the prototype problem of Gibbs oscillation. Consider a nonperiodic analytic function $f(x)$ in $[-1,1]$. Now, assume that the point values $f(x_j)$, where $x_j=2j/N$, $j=0,\ldots,N-1$, are known but the function $f(x)$ is not. This is equivalent to knowing the first N discrete Fourier coefficients $\tilde{f}_k$, $-N/2\leqslant k\leqslant N/2-1$, of the function $f(x)$ defined by

$$\tilde{f}_k = \sum_{j=0}^{N-1} f(x_j) e^{-i\pi k x_j}. \tag{27}$$

Then the classical Fourier sum

$$f_N(x) = \sum_{k=-N/2}^{N/2-1} \tilde{f}_k e^{i\pi k x} \tag{28}$$

reconstructs the point values everywhere in $-1 \leqslant x \leqslant 1$.

The finite Fourier expansion converges exponentially as N increases when the approximated function is analytic (i.e., infinitely smooth) and periodic [14]. If $f(x)$ is either discontinuous or nonperiodic, however, then $f_N(x)$ is not a good approximation to $f(x)$. Away from the discontinuity or the boundary, the convergence is only $O(\frac{1}{N})$, and there is an overshoot close to the discontinuity or the boundary that does not diminish with increasing N [14]; this is referred to as the Gibbs phenomenon [12]. The phenomenon manifests itself in many situations, including the problem we present in this paper.

Gottlieb et al. showed in a series of papers that, knowing the first N Fourier coefficients, one can reconstruct a *rapidly converging* series based on the expansions in Gegenbauer polynomials (see [16] for references). The point values of $f(x)$ everywhere in $-1 \leqslant x \leqslant 1$ can be recovered with exponential accuracy in the maximum norm up to the discontinuity or the boundary.

The Gegenbauer series for the function $f(x)$, based on the Gegenbauer polynomials $C_n^\alpha(x)$, which are orthogonal over the range $x \in [-1,1]$ with the weight function $(1-x^2)^{\alpha-\frac{1}{2}}$ for any constant $\alpha \geqslant 0$, is defined by

$$f(x) = \sum_{n=0}^{\infty} \hat{b}_n^\alpha C_n^\alpha(x), \tag{29}$$

where the continuous Gegenbauer coefficient is defined by

$$\hat{b}_n^\alpha = \frac{1}{h_n^\alpha} \int_{-1}^{1} (1-x^2)^{\alpha-\frac{1}{2}} C_n^\alpha(x) f(x)\, dx \tag{30}$$

with the normalization constant

$$h_n^\alpha = \pi^{\frac{1}{2}} C_n^\alpha(1) \frac{\Gamma(\alpha+\frac{1}{2})}{\Gamma(\alpha)(n+\alpha)} \quad \text{and} \quad C_n^\alpha(1) = \frac{\Gamma(n+2\alpha)}{n!\Gamma(2\alpha)}. \tag{31}$$

The finite sum of the first $M+1$ terms of the Gegenbauer expansion in (29), denoted by

$$g_M^\alpha(x) = \sum_{n=0}^{M} \hat{b}_n^\alpha C_n^\alpha(x), \tag{32}$$

converges exponentially to an analytic function $f(x)$ in $[-1,1]$. The convergence rate of the infinite series depends on the rate of decay in the magnitude of the coefficients.

In practice, the continuous coefficients $\hat{b}_n^\alpha$ must be computed; they are computed in a discrete sense. Assume that we are given only an approximation of $f(x)$, the Fourier pseudospectral data, in our problem. It was shown that the Fourier finite expansion (28) can be used to approximate $\hat{b}_n^\alpha$. Now we define the discrete Gegenbauer coefficients b_n^α, instead of the continuous Gegenbauer coefficients $\hat{b}_n^\alpha$, by substituting $f(x)$ by $f_N(x)$ in (30). Then the discrete Gegenbauer finite expansion is expressed as

$$g_{M,N}^\alpha(x) = \sum_{n=0}^{M} b_n^\alpha C_n^\alpha(x), \tag{33}$$

where the discrete Gegenbauer coefficients are defined by using $f_N(x)$ as follows:

$$b_n^\alpha = \frac{1}{h_n^\alpha} \int_{-1}^{1} (1-x^2)^{\alpha-\frac{1}{2}} C_n^\alpha(x) f_N(x)\, dx. \tag{34}$$

In fact, one can represent the discrete Gegenbauer coefficient in terms of the discrete Fourier coefficients. Plugging (28) into (34), one obtains

$$b_n^\alpha = \sum_{k=-\frac{N}{2}}^{\frac{N}{2}-1} \tilde{f}_k \left(\frac{1}{h_n^\alpha} \int_{-1}^{1} (1-x^2)^{\alpha-\frac{1}{2}} C_n^\alpha(x) e^{i\pi k x} \, dx \right), \tag{35}$$

where the integration part has an explicit form [3] for $k \neq 0$ as

$$\frac{1}{h_n^\alpha} \int_{-1}^{1} (1-x^2)^{\alpha-\frac{1}{2}} C_n^\alpha(x) e^{i\pi k x} \, dx = \Gamma(\alpha) \left(\frac{2}{k\pi} \right)^\alpha i^n (n+\alpha) J_{n+\alpha}(k\pi), \tag{36}$$

where $\Gamma(x)$ is the gamma function and $J_n(x)$ is the Bessel function of first kind. For $k = 0$, one uses the orthogonal property of the Gegenbauer polynomials. Thus, we have

$$b_n^\alpha = \tilde{f}_0 \delta_{0n} + \sum_{k=-\frac{N}{2}, k\neq 0}^{\frac{N}{2}-1} \tilde{f}_k \Gamma(\alpha) \left(\frac{2}{k\pi} \right)^\alpha i^n (n+\alpha) J_{n+\alpha}(k\pi). \tag{37}$$

A rigorous proof of the exponential convergence of the Gegenbauer approximation (33) to an analytic function $f(x)$ is shown in [15,16]. Note that, for a fixed α and N, the approximation $g_{M,N}^\alpha$ converges to $f_N(x)$ as M increases to infinity, which is not the desired result. Rather, one must consider simultaneous variations in M, α, and N to achieve the exponential convergence.

In applications, the number of Fourier coefficients, N, is fixed. Thus, α and M are free parameters to be chosen depending on N and on the size of each subdomain. The optimum relation between the parameters and other factors has been analyzed analytically in [16]. However, these analytical results are not sufficient for providing a practical algorithm. There is also the need for further numerical experimentation. For this paper we carry out a variety of calculations and, based on our empirical observations (Section 5), present some rough guidelines for parameter choices.

In the following sections, we discuss the detailed procedures in one dimension and two dimensions.

4.1. Reconstructions in one dimension

Consider a piecewise analytic function $f(x)$ that is integrable in $[0,L]$. Suppose that $f(x)$ has known discontinuities at $x = d_0$ and $x = d_1$ in $[0,L]$. Then we divide the global domain into three subdomains, denoted by $\Omega_1 = [0,d_0]$, $\Omega_2 = [d_0,d_1]$, and $\Omega_2 = [d_1,L]$, and carry out the Gegenbauer reconstruction in each subdomain. First, we define a set of grids in the global domain defined by $x_j = Lj/N$, $j = 0,1,\ldots,N-1$ and assume that the point values $f(x_j)$ $(j = 0,1,\ldots,N-1)$ are given. Then we obtain the Fourier coefficients $\tilde{f}_k (-\frac{N}{2} \leqslant k \leqslant \frac{N}{2} - 1)$ by applying a discrete fast Fourier transform, so that the classical Fourier finite sum everywhere in $[0,L]$ is defined by

$$f_N(x) = \sum_{k=-\frac{N}{2}}^{\frac{N}{2}-1} \tilde{f}_k e^{i\frac{2\pi k}{L}x}. \tag{38}$$

Let us denote a subdomain by $\Omega_s = [a,b]$ and define a local variable, for $\xi \in [-1,1]$, $x^s = \frac{(b-a)}{2}\xi + \frac{(b+a)}{2}$. Let $\epsilon = \frac{b-a}{L}$ and $\delta = \frac{b+a}{L}$. The Fourier finite sum using the variable ξ is

$$f_N(x^s(\xi)) = \sum_{k=-\frac{N}{2}}^{\frac{N}{2}-1} \tilde{f}_k e^{i\pi k(\epsilon\xi+\delta)}. \tag{39}$$

Now we define the Gegenbauer coefficients in each subdomain

$$b_n^{\Omega_s} = \frac{1}{h_n^\alpha} \int_{-1}^{1} (1-\xi^2)^{\alpha-\frac{1}{2}} C_n^\alpha(\xi) f_N(x^s(\xi)) \, d\xi. \tag{40}$$

Then, plugging (39) into (40) and using the explicit formula (36) for the integration part, we denote:

$$\text{For } k \neq 0, \quad B^{\Omega_s}_{n,k} = \frac{e^{i\pi k\delta}}{h^{\alpha}_n} \int_{-1}^{1} (1-\xi^2)^{\alpha-\frac{1}{2}} C^{\alpha}_n(\xi) e^{i\pi k\epsilon\xi}\, d\xi = e^{i\pi k\delta}\Gamma(\alpha)\left(\frac{2}{k\pi\epsilon}\right)^{\alpha} i^n (n+\alpha) J_{n+\alpha}(k\epsilon\pi),$$
$$\text{For } k = 0, \quad B^{\Omega_s}_{n,k} = \delta_{nk}. \tag{41}$$

Then, the local Gegenbauer coefficients are expressed in a matrix form

$$\begin{bmatrix} b^{\Omega_s}_0 \\ b^{\Omega_s}_1 \\ \cdot \\ \cdot \\ b^{\Omega_s}_M \end{bmatrix} = \begin{bmatrix} B^{\Omega_s}_{0,-\frac{N}{2}} & B^{\Omega_s}_{0,-\frac{N}{2}+1} & \cdots & B^{\Omega_s}_{0,\frac{N}{2}-1} \\ B^{\Omega_s}_{1,-\frac{N}{2}} & B^{\Omega_s}_{1,-\frac{N}{2}+1} & \cdots & B^{\Omega_s}_{1,\frac{N}{2}-1} \\ \cdot & \cdot & \cdots & \cdot \\ \cdot & \cdot & \cdots & \cdot \\ B^{\Omega_s}_{M,-\frac{N}{2}} & B^{\Omega_s}_{M,-\frac{N}{2}} & \cdots & B^{\Omega_s}_{M,\frac{N}{2}-1} \end{bmatrix} \begin{bmatrix} \tilde{f}_{-\frac{N}{2}} \\ \tilde{f}_{-\frac{N}{2}+1} \\ \cdot \\ \cdot \\ \tilde{f}_{\frac{N}{2}-1} \end{bmatrix}.$$

Next, we evaluate the point values in each subdomain as follows. Let $\mathbf{x}^s = \{x^s_i, \ldots, x^s_j\}$ be a subset of $\{x_j\}_{j=0}^{N-1}$, which is in Ω_s. We use the cost-effective version of the Gegenbauer reconstruction technique that defines the Gegenbauer polynomials in terms of trigonometric functions [1,3,24]. In this case, for $x_s = \cos\theta$, we have:

$$C^{\alpha}_n(\cos\theta) = \sum_{m=0}^{n} a^{\alpha}_{m,n} \cos(n-2m)\theta \tag{42}$$

and

$$a^{\alpha}_{m,n} = \frac{\Gamma(\alpha+m)\Gamma(\alpha+n-m)}{m!(n-m)!\Gamma^2(\alpha)}, \tag{43}$$

where Γ is the gamma function. Define $T^s_{i,m} = \cos[m(\cos^{-1}\xi_i)]$ for $\xi_i = \frac{2}{b-a}x^s_i - \frac{b+a}{b-a}$. Note that the Gegenbauer coefficients are newly computed in each subdomain and that the reconstructed point values, denoted by $\mathbf{g}^{\Omega_s}_i$, on grid set $\mathbf{x}^s$ in each subdomain are obtained by

$$\begin{bmatrix} \mathbf{g}^{\Omega_s}_i \\ \cdot \\ \cdot \\ \cdot \\ \cdot \\ \mathbf{g}^{\Omega_s}_j \end{bmatrix} = \begin{bmatrix} T^s_{i,0} & T^s_{i,1} & \cdots & T^s_{i,M} \\ \cdot & \cdot & \cdots & \cdot \\ \cdot & \cdot & \cdots & \cdot \\ \cdot & \cdot & \cdots & \cdot \\ \cdot & \cdot & \cdots & \cdot \\ T^s_{j,0} & T^s_{j,1} & \cdots & T^s_{j,M} \end{bmatrix} \begin{bmatrix} a^{\alpha}_{00} & 0 & a^{\alpha}_{12} & 0 & \cdots & a^{\alpha}_{\frac{M}{2},M} \\ 0 & 2a^{\alpha}_{01} & 0 & 2a^{\alpha}_{13} & \cdots & 0 \\ 0 & 0 & 2a^{\alpha}_{02} & 0 & \cdots & 0 \\ \cdot & \cdot & 0 & \cdot & \cdots & 2a^{\alpha}_{1M} \\ \cdot & \cdot & \cdot & 0 & \cdots & 0 \\ 0 & 0 & 0 & 0 & 0 & 2a^{\alpha}_{0M} \end{bmatrix} \begin{bmatrix} b^{\Omega_s}_0 \\ b^{\Omega_s}_1 \\ \cdot \\ \cdot \\ \cdot \\ b^{\Omega_s}_M \end{bmatrix}.$$

Let N^s be the number of the elements in $\mathbf{x}^s$ and D the number of discontinuities. Then the first $N^s \times (M+1)$ matrix in the right-hand side of the equation above is denoted by $\mathbf{T}^s$ and the second $(M+1)\times(M+1)$ matrix by $\mathbf{A}^s$. Then

$$\mathbf{g}^s = \mathbf{T}^s\mathbf{A}^s\mathbf{b}^s, \tag{44}$$

where $\mathbf{g}^s = [g^{\Omega_s}_i, \ldots g^{\Omega_s}_j]^{\mathrm{T}}$ and $\mathbf{b}^s = [b^{\Omega_s}_0, b^{\Omega_s}_1, \ldots, b^{\Omega_s}_M]^{\mathrm{T}}$. The number of operations for the matrix–vector multiplication $\mathbf{A}^s\mathbf{b}^s$ is $\frac{(M+2)(M+4)}{4}$. However, one has to compute this procedure for each subdomain, so the amount of work for this procedure is $\mathscr{M}^S = \sum_{s=1}^{S} \frac{(M^s+2)(M^s+4)}{4}$, where $S\ (\geqslant D)$ stands for the number of subdomains. After multiplication with $\mathbf{T}^s$, the total amount of work is $\frac{N^s(M^s+2)(M^s+4)}{4}$ in each subdomain. Thus, denoted by $M_{\max} = \max\{M^s\}$, for $M_{\max} = \beta N$, $(0<\beta<1)$ (i.e., proportional to N), the total cost is $O(\frac{1}{4}\beta(S\beta+4)N^2)$. On the other hand, the conventional recurrence formula [1,3] costs $O(3S\beta N^2)$.

In summary, the reconstruction procedure in one dimension is as follows:

Step 1. Compute the first $M+1$ discrete Gegenbauer coefficients (40) in a subdomain.
Step 2. Construct the Gegenbauer finite sum (44) on the grids in the subdomain.
Step 3. Repeat Step 1 and Step 2 in the remaining subdomains, separately.

To show how the method performs with exponential convergence, we demonstrate some computational results for the following examples.

Example 1. Consider the following discontinuous function, and assume that we are given $N = 256$ and $N = 512$ discrete Fourier coefficients, as defined in (27), for each function:

$$f_1(x) = \begin{cases} x^3 - x^2 + 2 & (-1 \leqslant x \leqslant -\frac{1}{2}), \\ x^2 + 5 & (-\frac{1}{2} \leqslant x \leqslant \frac{1}{2}), \\ x^3 - 2 & (\frac{1}{2} \leqslant x \leqslant 1). \end{cases} \tag{45}$$

Fig. 2 shows the Fourier approximations, their reconstructed results, and the pointwise errors for the functions. For discontinuous functions, the standard Fourier approximation gives only $O(\frac{1}{N})$ convergence away from the discontinuities and O(1) convergence near the discontinuities, as shown in the error plots as dashed lines. Reconstructions are carried out for the function with three subdomains whose interfaces are indicated by the vertical dotted lines. In the error plot, the parameters M and α are assigned as proportional to $O(N^{\frac{1}{3}})$; that is, $M = 6$, $\alpha = 6$ in each subdomain for a fixed $N = 256$ (dotted line) and $M = 8$, $\alpha = 8$ for $N = 512$ (solid line). With other parameters M and α proportional to $O(N^{\frac{1}{p}})$, $p = 2, \ldots, 8$, the accuracy was successfully improved compared to the Fourier result (dashed line).

Example 2. Consider the following piecewise analytic function $f_2(x)$, and assume that we are given only $N = 256$ and $N = 512$ discrete Fourier coefficients:

$$f_2(x) = \begin{cases} (x + 0.43)^2 & (-1 \leqslant x < -0.43), \\ 40(x + 0.43)^2 & (-0.43 \leqslant x < -0.33), \\ 10(x + 0.23)^2 & (-0.33 \leqslant x < -0.23), \\ -5(x^2 - 0.0529) & (-0.23 \leqslant x < 0.23), \\ -5(x - 0.23)^2 & (0.23 \leqslant x < 0.33), \\ -30(x - 0.43)^2 & (0.33 \leqslant x < 0.43), \\ 0.5(x - 0.43)^2 & (0.43 \leqslant x \leqslant 1). \end{cases} \tag{46}$$

Fig. 2 shows the Fourier approximation, its reconstructed result, and the pointwise errors. Reconstructions are carried out with seven subdomains whose interfaces are indicated by the vertical dotted lines. For the Fourier data with $N = 256$, parameters are chosen as $M = O(N^{\frac{1}{5}}) = 3$ and $\alpha = O(N^{\frac{1}{4}}) = 4$, whose pointwise error is shown with a dotted line. The errors for the small subdomains around the singularities shows only 1-digit accuracy in the maximum norm for the case with $N = 256$. For the Fourier data with $N = 512$, parameters are chosen as $M = O(N^{\frac{1}{4}}) = 4$ and $\alpha = O(N^{\frac{1}{3}}) = 8$, whose pointwise error is shown with a solid line. The errors for the small subdomains around the singularities decay with 4-digit accuracy in maximum norm when the resolution is as large as $N = 512$. In the cases $N = 256$ with other parameters for the small subdomains around the singularities, the parameters could be chosen as $M = 2$ with $\alpha = 2, 3, 4, 6, 16$, $M = 3$ with $\alpha = 3, 4, 6$, and $M = 4$ with $\alpha = 4, 6$; these cases all successfully improved the accuracy compared to the Fourier result, at least with more than 1-digit accuracy in the maximum norm. However, $M = O(N^{\frac{1}{p}})$, $p = 2, 3$ with any $\alpha = O(N^{\frac{1}{q}})$, $q \geqslant 2$ does not improve the O(1) accuracy of the Fourier approximation.

Remark 1. From Examples 1 and 2, we observe that for desired reconstructions with at least 1-digit accuracy in maximum norm, the size of the smallest subdomain restricts the range of M, which we empirically set to be proportional to $O(N^{\frac{1}{p}})$, $p \geqslant 2$. Accordingly, we set α to be proportional to $O(N^{\frac{1}{p}})$. For the application problem in this paper with no analytic solution, we will choose the parameters in a similar manner. Within the narrower range for M and α, we choose a relatively good solution from among the reconstructed solutions. We leave as future work intensive study on the regular pattern for the relation in parameters with an automatic measure for the quality of reconstructed solutions.

Remark 2. Reconstructions require computing the Gegenbauer coefficients in each subdomain. We first examine the computation time to obtain a set of the $(M + 1)$ Gegenbauer coefficients with N Fourier data in a single subdomain. Fig. 3 shows the cases of $M = 1, \ldots, 20$ for $N = 32, 64, 128, 256$ for a fixed $\alpha = 1$ with solid lines. Theoretically, the computation time does not depend on the increasement with α. In our computational implementation, for different α, the CPU time is scaled by a small constant number when α increases. For example, the case

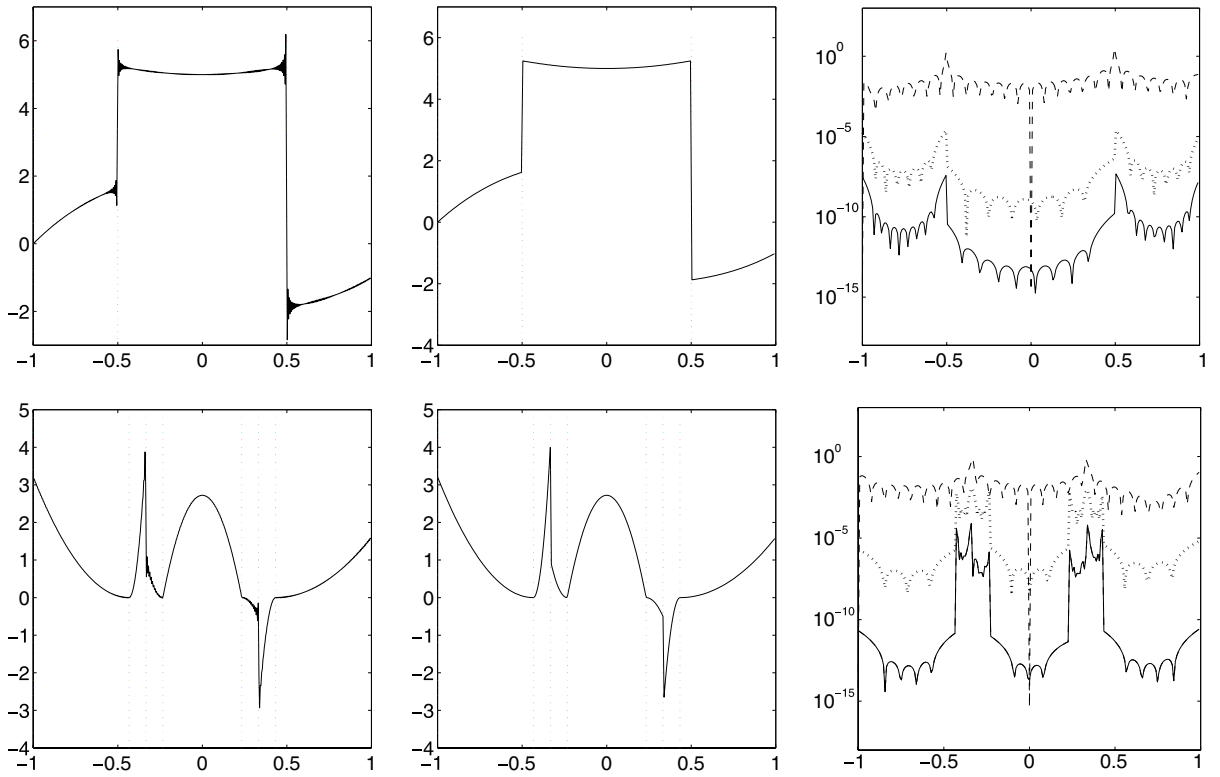

Fig. 2. From the left column: Fourier approximations, their Gegenbauer reconstructions, and pointwise errors. The vertical dotted lines indicate the interfaces of subdomains. Parameters in the pointwise errors for $f_1(x)$ (first row): $M = 6$ and $\alpha = 6$ for 3 subdomains and $N = 256$ (dotted line); $M = 8$ and $\alpha = 8$, and $N = 512$ (solid line). Parameters in the pointwise errors for $f_2(x)$ (second row): $M = 3$, $\alpha = 4$ for 7 subdomains, and $N = 256$ (dotted line); $M = 4$, $\alpha = 8$, and $N = 512$ (solid line). The dashed lines in the error plots are for Fourier approximations.

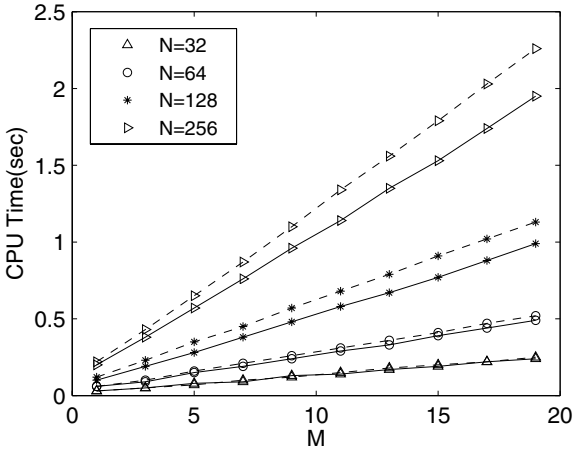

Fig. 3. CPU times on an AMD Athlon of 1 GHz for computing the $(M + 1)$ Gegenbauer coefficients with the parameters $M = 1, \ldots, 20$ and $N = 32$, 64, 128, 256. The solid lines are for $\alpha = 1$ and the dashed lines are for $\alpha = 20$.

with $\alpha = 20$ is shown with dashed lines in Fig. 3. One can estimate the total reconstruction time as follows. If the CPU time to perform a one-subdomain reconstruction is $\tau^s_{M,N}$, then the total cost to perform this reconstruction in the global domain is $\sum_{s=1}^{S} \tau^s_{M,N}$, which is in fact proportional to the time obtained by multiplying the number of the subdomains to the maximum of the subdomain reconstruction CPU times, that is, τS, where $\tau = \max_s\{\tau^s_{M,N}\}$.

4.2. Reconstructions in two dimensions

In this section, we extend the use of the cost-effective version of the Gegenbauer reconstruction technique to two-dimensional problems. The Gegenbauer finite sum in two dimensions has the following form. For $x=\cos\theta_x$, $y=\cos\theta_y$ in a domain $\Omega=[-1,1]^2$, denoting $\alpha=(\alpha_x,\alpha_y)$, $\mathbf{M}=(M_x,M_y)$ and $\mathbf{N}=(N_x,N_y)$, we have

$$g^{\alpha}_{\mathbf{M},\mathbf{N}}(x,y)=\sum_{m_x=0}^{M_x}\sum_{m_y=0}^{M_y} b^{\alpha}_{m_x,m_y}C^{\alpha_x}_{m_x}(x)C^{\alpha_y}_{m_y}(y). \tag{47}$$

The coefficients $b^{\alpha}_{m_x,m_y}$ for the Gegenbauer finite sum in two dimensions are defined by

$$b^{\alpha}_{m_x,m_y}=\frac{1}{h^{\alpha_x}_{m_x}h^{\alpha_y}_{m_y}}\int_{-1}^{1}\int_{-1}^{1}(1-x^2)^{\alpha_x-\frac{1}{2}}(1-y^2)^{\alpha_y-\frac{1}{2}}C^{\alpha_x}_{m_x}(x)C^{\alpha_y}_{m_y}(y)f_N(x,y)\,\mathrm{d}x\,\mathrm{d}y. \tag{48}$$

Consider the computational domain $[0,L_x]\times[0,L_y]$, and define a set of grids $x_{\hat{i}}=\frac{L\hat{i}}{N_x}$ $(\hat{i}=0,\ldots,N_x-1)$ and $y_{\hat{j}}=\frac{L\hat{j}}{N_y}$ $(\hat{j}=0,\ldots,N_y-1)$. Now, assume that the point values $f(x_{\hat{i}},y_{\hat{j}})$ are known but the function $f(x,y)$ is not. Then the discrete Fourier coefficients $\tilde{f}_{k_x,k_y}$, $-\frac{N}{2}\leqslant k_x,k_y\leqslant\frac{N}{2}-1$ (for $N=N_x=N_y$) are obtained by

$$\tilde{f}_{k_x,k_y}=\sum_{\hat{i}=0}^{N-1}\sum_{\hat{j}=0}^{N-1}f(x_{\hat{i}},y_{\hat{j}})\mathrm{e}^{-\mathrm{i}\frac{2\pi k_x}{L_x}x_{\hat{i}}}\mathrm{e}^{-\mathrm{i}\frac{2\pi k_y}{L_y}y_{\hat{j}}}, \tag{49}$$

and the two-dimensional Fourier finite sum everywhere in $\Omega=[0,L_x]\times[0,L_y]$ is

$$f_N(x,y)=\sum_{k_x=-\frac{N}{2}}^{\frac{N}{2}-1}\sum_{k_y=-\frac{N}{2}}^{\frac{N}{2}-1}\tilde{f}_{k_x,k_y}\mathrm{e}^{\mathrm{i}\frac{2\pi k_x}{L_x}x}\mathrm{e}^{\mathrm{i}\frac{2\pi k_y}{L_y}y}. \tag{50}$$

Let us denote a subdomain by $\Omega_{s,t}=[a_x,b_x]\times[a_y,b_y]$, where a_x and b_x are the known discontinuities in the x-direction and a_y and b_y in the y-direction. Define local variables for $\xi,\eta\in[-1,1]\times[-1,1]$, $x^s=\frac{(b_x-a_x)}{2}\xi+\frac{(b_x+a_x)}{2}$ and $y^t=\frac{(b_y-a_y)}{2}\eta+\frac{(b_y+a_y)}{2}$. Let $\epsilon_x=\frac{b_x-a_x}{L_x}$, $\delta_x=\frac{b_x+a_x}{L_x}$, $\epsilon_y=\frac{b_y-a_y}{L_y}$, and $\delta_y=\frac{b_y+a_y}{L_y}$. Then the Fourier finite sum in the subdomain $\Omega_{s,t}$ is expressed by

$$f_N(x^s(\xi),y^t(\eta))=\sum_{k_x=-\frac{N}{2}}^{\frac{N}{2}-1}\sum_{k_y=-\frac{N}{2}}^{\frac{N}{2}-1}\tilde{f}_{k_x,k_y}\mathrm{e}^{\mathrm{i}\pi k_x(\epsilon_x\xi+\delta_x)}\mathrm{e}^{\mathrm{i}\pi k_y(\epsilon_y\eta+\delta_y)}. \tag{51}$$

Plugging (49) into (51), we have

$$\begin{aligned}f_N(x^s(\xi),y^t(\eta))&=\sum_{k_y=-\frac{N}{2}}^{\frac{N}{2}-1}\sum_{\hat{j}=0}^{N-1}\left[\sum_{k_x=-\frac{N}{2}}^{\frac{N}{2}-1}\left(\sum_{\hat{i}=0}^{N-1}f(x_{\hat{i}},y_{\hat{j}})\mathrm{e}^{-\mathrm{i}\frac{2\pi k_x}{L_x}x_{\hat{i}}}\right)\mathrm{e}^{\mathrm{i}\pi k_x x^s(\xi)}\right]\mathrm{e}^{-\mathrm{i}\frac{2\pi k_y}{L_y}y_{\hat{j}}}\mathrm{e}^{\mathrm{i}\pi k_y y^t(\eta)}\\&=\sum_{k_y=-\frac{N}{2}}^{\frac{N}{2}-1}\left(\sum_{\hat{j}=0}^{N-1}f_N(x^s(\xi),y_{\hat{j}})\mathrm{e}^{-\mathrm{i}\frac{2\pi k_y}{L_y}y_{\hat{j}}}\right)\mathrm{e}^{\mathrm{i}\pi k_y y^t(\eta)}\end{aligned} \tag{52}$$

and the Gegenbauer coefficients in the subdomain $\Omega_{s,t}$ have the form

$$b^{\Omega_{s,t}}_{m_x,m_y}=\frac{1}{h^{\alpha_y}_{m_y}}\int_{-1}^{1}(1-y^2)^{\alpha_y-\frac{1}{2}}C^{\alpha_y}_{m_y}(\eta)\left[\sum_{k_y=-\frac{N}{2}}^{\frac{N}{2}-1}\left(\sum_{\hat{j}=0}^{N-1}\mathbf{b}^{\Omega_s}_{m_y}(m_x,y_{\hat{j}})\mathrm{e}^{-\mathrm{i}\frac{2\pi k_y}{L_y}y_{\hat{j}}}\right)\mathrm{e}^{\mathrm{i}\pi k_y y^t(\eta)}\right]\mathrm{d}\eta, \tag{53}$$

where

$$\mathbf{b}^{\Omega_s}_{m_y}(m_x,y_{\hat{j}})=\frac{1}{h^{\alpha_x}_{m_x}}\int_{-1}^{1}(1-\xi^2)^{\alpha_x-\frac{1}{2}}C^{\alpha_x}_{m_x}(\xi)f_N(x^s(\xi),y_{\hat{j}})\,\mathrm{d}\xi. \tag{54}$$

Then, for a fixed $y_{\hat{j}}$, the one-dimensional Gegenbauer reconstruction in the x-direction is written as

$$\mathbf{g}_{M_x}^{\Omega_{s,t}}(x^s(\xi), y_{\hat{j}}) = \sum_{m_x=0}^{M_x} \mathbf{b}_{m_y}^{\Omega_s}(m_x, y_{\hat{j}}) C_{m_x}^{\alpha_x}(\xi). \tag{55}$$

The two-dimensional reconstruction form is

$$g_{M,N}^{\alpha}|_{\Omega_{s,t}} = g^{\Omega_{s,t}}(x^s(\xi), y^t(\eta)) = \sum_{m_y=0}^{M_y} b_{m_x,m_y}^{\Omega_{s,t}} C_{m_y}^{\alpha_y}(\eta), \tag{56}$$

where

$$b_{m_x,m_y}^{\Omega_{s,t}} = \frac{1}{h_{m_y}^{\alpha_y}} \int_{-1}^{1} (1-y^2)^{\alpha_y-\frac{1}{2}} C_{m_y}^{\alpha_y}(\eta) \left[\sum_{k_y=-\frac{N}{2}}^{\frac{N}{2}-1} \left(\sum_{\hat{j}=0}^{N-1} \mathbf{g}_{M_x}^{\Omega_{s,t}}(x^s(\xi), y_{\hat{j}}) \mathrm{e}^{-\mathrm{i}\frac{2\pi k_y}{L_y} y_{\hat{j}}} \right) \mathrm{e}^{\mathrm{i}\pi k_y y^t(\eta)} \right] \mathrm{d}\eta.$$

Then the local Gegenbauer coefficients are given in matrix form as

$$b^{\Omega_{s,t}} = \mathbf{B}_y^{\Omega^t} \tilde{\mathbf{f}} \left(\mathbf{B}_x^{\Omega^s} \right)^{\mathrm{T}}, \tag{57}$$

where $b^{\Omega_{s,t}} = [b_{m_x,m_y}^{\Omega_{s,t}}]$, $\tilde{\mathbf{f}} = [\tilde{f}_{k_y,k_x}]$, $\mathbf{B}_x^{\Omega^s} = [B_{m_x,k_x}^{\Omega^s}]$, and $\mathbf{B}_y^{\Omega^t} = [B_{m_y,k_y}^{\Omega^t}]$, as defined in (42). Finally, the two-dimensional Gegenbauer reconstruction can be summarized in matrix form as follows:

$$g^{s,t} = [\mathbf{T}_y^t \mathbf{A}_y^t (\mathbf{T}_x^s \mathbf{A}_x^s b^{\Omega_{s,t}})^{\mathrm{T}}]^{\mathrm{T}} = \mathbf{T}_x^s \mathbf{A}_x^s (b^{\Omega_{s,t}}) (\mathbf{A}_y^t)^{\mathrm{T}} (\mathbf{T}_y^t)^{\mathrm{T}}, \tag{58}$$

where $g^{s,t} = [g_{\hat{i},\hat{j}}^{\Omega_{s,t}}]^{\mathrm{T}}$, $\mathbf{T}_x^s = [T_{\hat{i},m}^s] = [\cos(m(\cos^{-1}\xi_{\hat{i}}))]$, and $\mathbf{T}_y^t = [T_{\hat{j},m}^t] = [\cos(m(\cos^{-1}\eta_{\hat{j}}))]$ for $\xi_{\hat{i}} = \frac{2}{b_x-a_x}\xi_{\hat{i}}^s - \frac{b_x+a_x}{b_x-a_x}$, and $\eta_{\hat{j}} = \frac{2}{b_y-a_y}\eta_{\hat{j}}^t - \frac{b_y+a_y}{b_y-a_y}$, respectively.

A practical way to perform the two-dimensional reconstruction is that we need to perform only the one-dimensional procedure. The analysis program for the two-dimensional problem is the same as the one for one-dimensional problem, with an outside "for" loop. We first perform a one-dimensional reconstruction, say, in the x-direction. Obtaining one-dimensional Fourier data in the other direction (say in the y-direction), we then perform a reconstruction in the other direction:

Step 1. Compute the one-dimensional discrete Fourier coefficients w.r.t. x for a $y_{\hat{j}}$.
Step 2. Compute the first $M+1$ discrete Gegenbauer coefficients in a subdomain.
Step 3. Construct the Gegenbauer finite sum on the grids in the subdomain.
Step 4. Repeat Steps 2–3 in the remaining subdomains, separately, for the fixed $y_{\hat{j}}$.
Step 5. Repeat Steps 1–4 for each $y_{\hat{j}}$, and store all the data for the next step.
Step 6. Compute the one-dimensional discrete Fourier coefficients w.r.t. y for a $x_{\hat{i}}$.
Step 7. Repeat Steps 2–5 for all $x_{\hat{i}}$, separately.

5. Computational results

This section presents detailed numerical results obtained by the PSTD method and the Gegenbauer post-processing of these results.

We focus on the local domain Ω =[640 nm, 895 nm]×[128 nm, 383 nm], the region within the dotted lines of Fig. 1. Redefining the local domain Ω in a reference domain $\hat{\Omega} = [-128\text{ nm}, 127\text{ nm}] \times [-128\text{ nm}, 127\text{ nm}]$, Fig. 4 displays, as dashed lines, the interfaces for the various subdomains within Ω in our Gegenbauer reconstructions and the solid lines indicate representative lines (not interfaces) along y with x held fixed at $x = x_0$, and along x with y held fixed at $y = y_0$. The horizontal line along x with $y = y_0$ involves five subdomains; two subdomains corresponding to x-values to the left of the circle, a subdomain corresponding to x-values within the circle, and two subdomains corresponding to x-values to the right of the circle. Similar remarks hold for the subdomains along the vertical solid line at $x = x_0$. On the other hand, solid lines along x or y that do not cross the circle involve three subdomains.

We first discuss time snapshots of the field components E_x and E_y, Figs. 5–8. For generating the time snapshots, a sinusoidal wave hard source with frequency $\omega_0 = \frac{2\pi c}{\lambda_0}$ corresponding to $\lambda_0 = 340$ nm, modulated by a

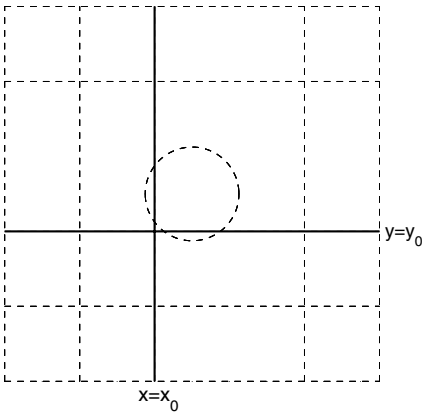

Fig. 4. Subdomains of a reference domain, $\hat{\Omega} = [-128\text{ nm}, 128\text{ nm}] \times [-128\text{ nm}, 128\text{ nm}]$, for the two-dimensional metal cylinder problem. The dashed lines are the interfaces of the subdomains, with the dashed circle corresponding to the metal cylinder boundary. The solid lines are representative lines along x and y for analyses in one-dimensional cuts. $x_0 = -128\text{ nm} + i\Delta x$, $i = 0,\ldots,N-1$ and $y_0 = -128\text{ nm} + j\Delta y$, $j = 0,\ldots,N-1$.

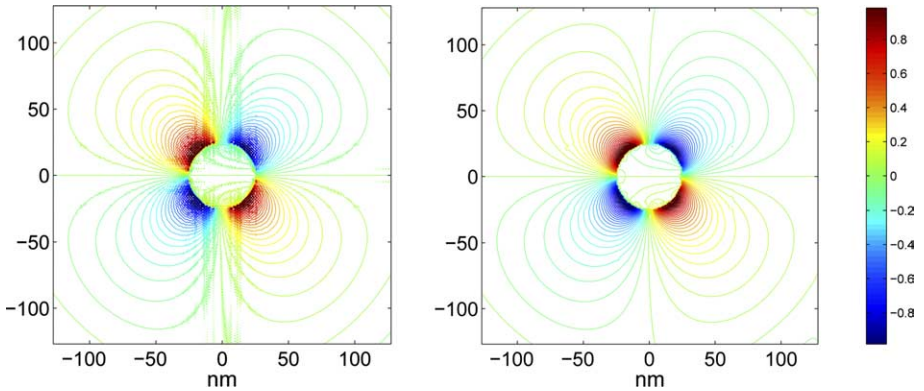

Fig. 5. Snapshots of E_x at time $= 11.48\text{e} - 15$ s with $\Delta t = 1.3514\text{e} - 18$. From the left, PSTD solution (7669.9 s) and Gegenbauer reconstruction (164.40 s).

17.5 fs. Blackman–Hariss window, is employed. This source is implemented at each field point along the source line depicted in Fig. 1 using the compact source approach in [22]. Overall, the incident wave generated from this source condition corresponds to an ultrashort laser pulse.

To ensure the numerical stability in time, we used [10,21,25]

$$\Delta t < \frac{2\sqrt{\epsilon_{\min}/\epsilon_0}}{\pi c\sqrt{1/\Delta x^2 + 1/\Delta y^2}}, \tag{59}$$

where $\epsilon_{\min} = \min\{\epsilon_0, \epsilon_0\epsilon_\infty\}$.

The snapshots in Figs. 5–8 were generated with spatial grid spacings $\Delta x = \Delta y = 1$ nm, corresponding to $N_x = 1024$, $N_y = 512$. The local domain defined by Ω represents a 256×256 cutout of the larger 1024×512 grids. The time step used was $\Delta t = 1.3514 \times 10^{-18}$ s, and the snapshots are at time $= 11.48 \times 10^{-15}$ s, which corresponds to a time such that the major part of the pulse is interacting with the metal cylinder.

In Figs. 5–8, the left-side figures are the PSTD results and the right-side figures are the Gegenbauer post-processed results. Figs. 6 and 8 show particular cuts along x and y of the results in Figs. 5 and 7. Nonphysical oscillations are evident in Figs. 5–8 for the PSTD results throughout the region of the cylinder and near this region. The Gegenbauer reconstructed results were carried out based on particular parameter choices for the Gegenbauer parameters, M and α, which may be different in each of the subdomains defined in Fig. 4. In

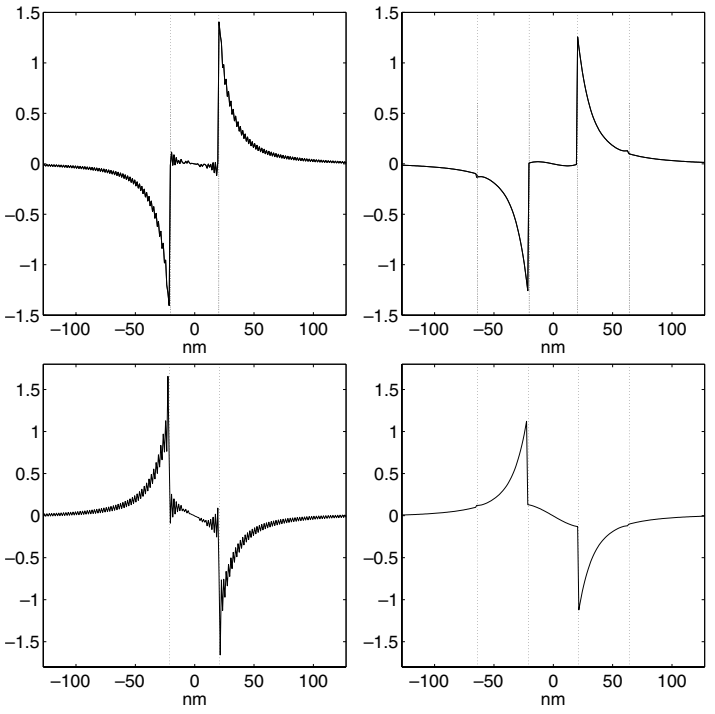

Fig. 6. One-dimensional slices of E_x: Dotted lines indicate the interfaces of the cylinder for the spectral (PSTD: left column) solution and the interfaces of subdomains for the Gegenbauer postprocessed (Gegenbauer: right column) solution. The top two panels are cuts along y with $x = -16$ nm, and the bottom two panels are cuts along x with $y = 14$ nm. The parameters for the Gegenbauer reconstruction are chosen as $M = 4$ and $\alpha = 6$ for the five subdomains.

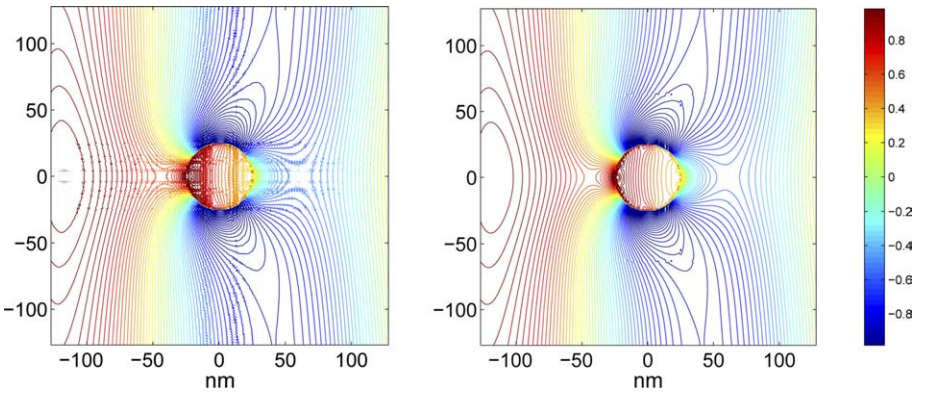

Fig. 7. Snapshots of E_y at time $= 11.48\,\mathrm{e}-15$ s with $\Delta t = 1.3514\mathrm{e}-18$. From the left, PSTD solution (7669.9 s) and Gegenbauer reconstruction (164.79 s).

Section 6, we outline an empirical procedure we found useful for choosing the parameters in each subdomain. Figs. 5–8 show that our Gegenbauer postprocessing technique successfully improves the PSTD results by eliminating all the nonphysical oscillations.

It is worthwhile to remark on the computational time associated with the reconstructions. For the snapshot calculations of Figs. 5–8, the PSTD simulation required approximately 2 h CPU time on an AMD Athlon 1 GHz. The cost-effective Gegenbauer reconstruction required less than 3 min, which is irrelevant in comparison to the simulation time.

In Figs. 9–11, we demonstrate the absolute magnitudes of frequency-domain field components, which are obtained by

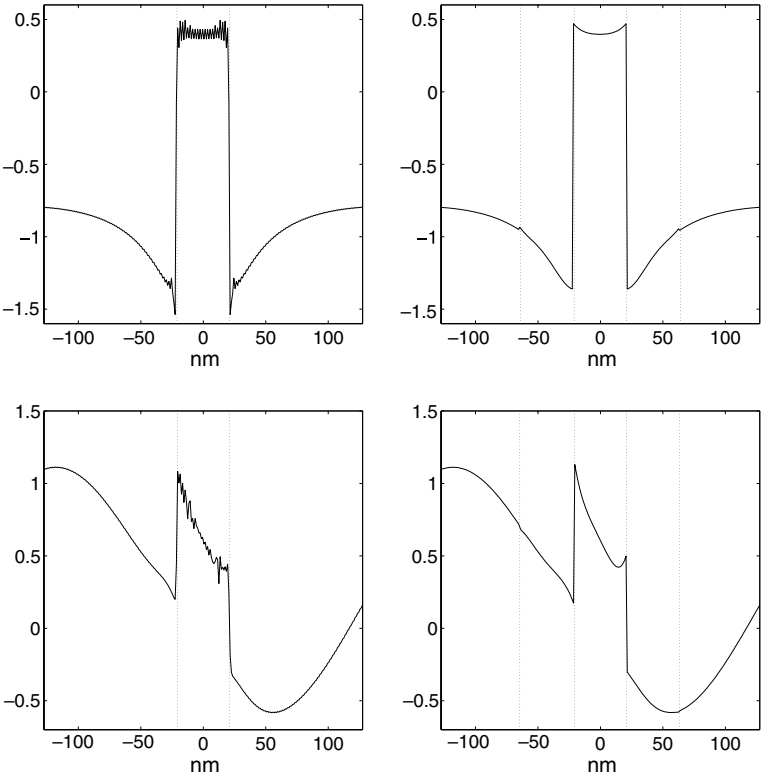

Fig. 8. One-dimensional slices of E_y: Dotted lines indicate the interfaces of the cylinder for the spectral (PSTD: left column) solution and the interfaces of subdomains for the Gegenbauer postprocessed (Gegenbauer: right column) solution. The top two panels are cuts along y with $x = 14$ nm, and the bottom two panels are cuts along x with $y = 14$ nm. The parameters for the Gegenbauer reconstruction are chosen as $M = 4$ and $\alpha = 6$ for five subdomains.

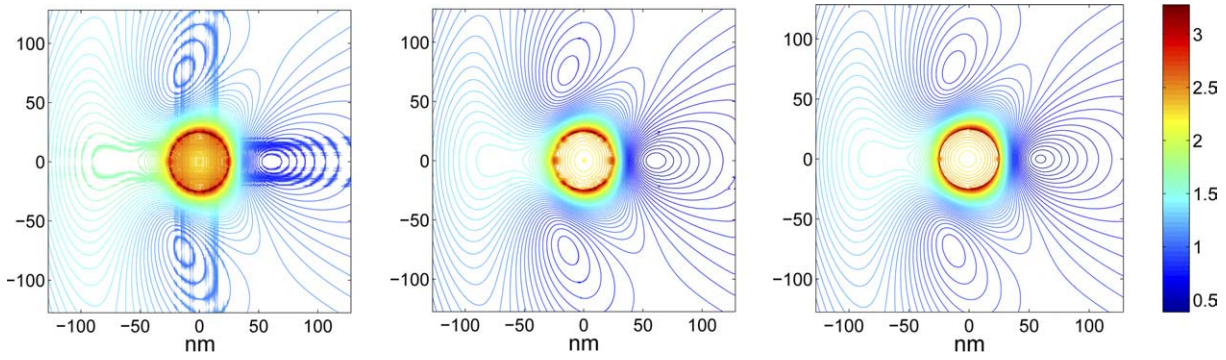

Fig. 9. Frequency-domain electric field magnitude in the Ω domain, $|\tilde{E}|$, corresponding to $\lambda_0 = 340$ nm: PSTD (left) and Gegenbauer (middle) with $\Delta x = \Delta y = 0.5$ nm and FDTD (right) with $\Delta x = \Delta y = 0.1$ nm.

$$\tilde{E}(x, y, \omega_0) = \int_0^\infty e^{i\omega_0 t} E(x, y, t)\, dt. \tag{60}$$

These field magnitudes can be interpreted as time-averaged field magnitudes, and are often the main focus in applications. We consider a frequency $\omega_0 = \frac{2\pi c}{\lambda_0}$, corresponding to $\lambda_0 = 340$ nm, although numerous other frequency components can be used.

In principle, one can evaluate Eq. (60) with time-domain results such as those discussed in Figs. 5–8. Accurate frequency-resolved results, however, involve a Fourier transformation over longer times than those of the

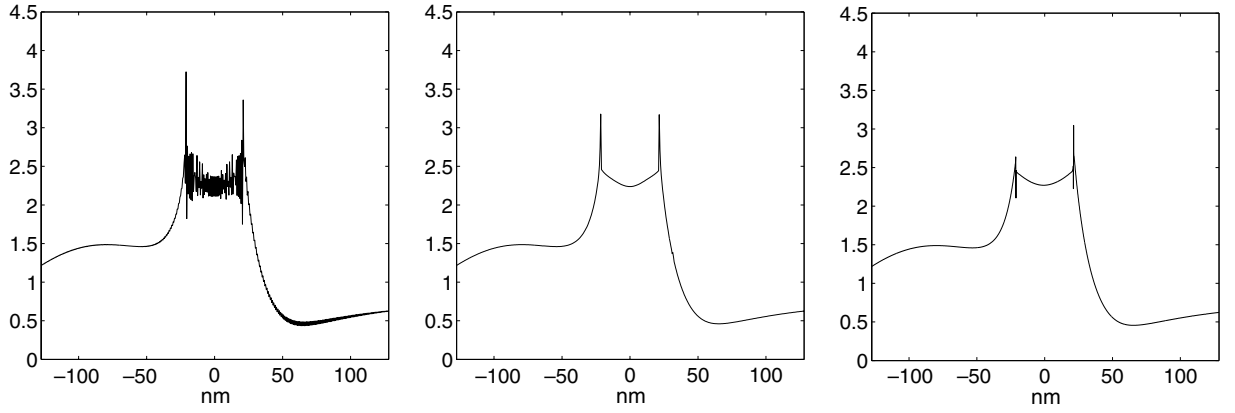

Fig. 10. One-dimensional slices in x-direction (with $y = 13$ nm) of the frequency-domain electric field magnitude, $|\tilde{E}|$, corresponding to $\lambda_0 = 340$ nm: PSTD (left) and Gegenbauer (middle) with $\Delta x = \Delta y = 0.5$ nm, and FDTD (right) with $\Delta x = \Delta y = 0.1$ nm.

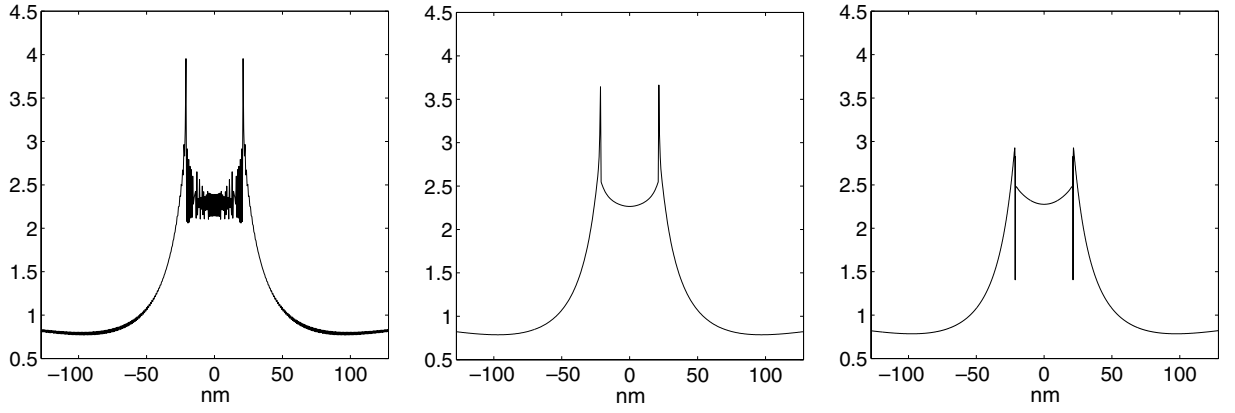

Fig. 11. One-dimensional slices in y-direction (with $x = 13$ nm) of the frequency-domain electric field magnitude, $|\tilde{E}|$, corresponding to $\lambda_0 = 340$ nm: PSTD (left) and Gegenbauer (middle) with $\Delta x = \Delta y = 0.5$ nm, and FDTD (right) with $\Delta x = \Delta y = 0.1$ nm.

snapshots, necessitating some care in the choice of initial conditions. In PSTD simulations, it is possible for waves that are reflected off the metal cylinder to reach the source and be artificially reflected back into the physical domain. The pulse width and final time should be chosen so that no such contamination occurs in the evaluation of Eq. (60) for the domain of interest, Ω. The particular initial source employed for the snapshots violates this requirement for the longer times of relevance here. We therefore used a shorter (4.3 fs) Blackman–Hariss window which did not lead to any back reflection errors in Ω.

Figs. 9–11 display some of our frequency-domain results. The PSTD results in the left-most panel of each figure were generated with a finer grid resolution, $\Delta x = \Delta y = 0.5$ nm. The central panel of each figure is the Gegenbauer reconstructed results. Due to the factor of two smaller grid spacings, the grid points within the local domain Ω are 512×512 for the Gegenbauer reconstructions. The right-most panel in each figure is the result of FDTD simulation with $\Delta x = \Delta y = 0.1$ nm. The very fine resolution of the FDTD simulation implies, apart from its behavior close to the metal/air interfaces, that this result should be very accurate (FDTD results with 0.2 nm resolution agree well with the 0.1 nm results, apart from the immediate vicinity of the metal/air boundaries).

Figs. 9–11 show that Gegenbauer reconstruction results are very close to the FDTD results. Thus, one can employ a grid spacing in the PSTD simulation that is five times larger than the one used for FDTD simulation, and obtain results in agreement with the finer resolution FDTD simulation, excluding the interface boundaries. Indeed, our reconstructed results very close to the metal/air interface are also physically more accept-

able, whereas the FDTD results exhibit the spurious downward spikes near the metal/air interface. The resolution $\Delta x = \Delta y = 0.5$ nm with PSTD simulation was required for the reconstructions to have good agreement to the FDTD results with the resolution of 0.1 nm.

6. Discussion

The Gegenbauer reconstruction in each subdomain requires estimates for the parameters M and α. From [13], we can expect that there is a range of parameters that gives good reconstructed results. Based on the numerical results in the previous sections, we outline an empirical procedure for identifying suitable parameter values. First, we restrict M and α to be $O(N^{\frac{1}{p}})$, $p \geqslant 2$. For example, for $N = 256$, of relevance to the snapshot calculations of the previous section, we have a set $P = \{1, 2, 3, 4, 6, 16\}$. Next, we choose the value of M from P to be proportional to the size of the relevant subdomain. The parameter α is then varied to obtain a smooth, physically acceptable result. Based on direct visual inspection of the results, we find that for subdomains involving large field variations, e.g. the regions near the metal/air interfaces, $\alpha \approx M$ yields the best results, whereas for subdomains with smooth field variations any $\alpha \in P$ is generally adequate.

For this reconstruction approach to become a robust practical tool, more automated algorithms for choosing M and α are required. This will involve the development of quantitative measures of the goodness of a reconstruction with particular M and α in comparison with other choices. It is possible that the smoothness indicators adapted from WENO method [29] could be of use, and the idea will be further discussed in a future paper.

7. Conclusion

We have presented a cost-effective Gegenbauer reconstruction technique applicable when one has a priori knowledge of the problem discontinuities. In one dimension, exponential convergence of the Gegenbauer reconstructions was demonstrated for a nonperiodic and some piecewise analytic functions. We extended the method to two dimensions and applied it as a postprocessing to the oscillatory Fourier pseudospectral solutions, which simulate electromagnetic waves interacting with a metallic nanowire where strong surface plasmon excitations can occur. Successful reduction of the oscillations in Fourier pseudospectral solutions is obtained after the Gegenbauer reconstructions. Comparisons of the reconstructed results to a finer resolution FDTD result are also provided. The Gegenbauer reconstructions provide reasonable profiles of the field response *up to* the metal surface, in contrast with the-finer resolution FDTD results.

Seeking an automated parameter-optimizing reconstruction method is an important goal for future work.

Acknowledgments

This work was supported in part by the Mathematics, Information, and Computational Science Division subprogram of the Office of Advanced Scientific Computing Research, Office of Science, and in part by the Office of Basic Energy Sciences, Division of Chemical Sciences, Geosciences, and Biosciences, under DOE contract W-31-109-ENG-38.

References

[1] M. Abramowitz, I.A. Stegun, Handbook of Mathematical Functions, Dover Publications, Inc., New York, 1970.
[2] W.L. Barnes, A. Dereux, T.W. Ebbensen, Surface plasmon subwavelength optics, Nature 424 (2003) 824–830.
[3] H. BatemanHigher Transcendental Functions, vol. 2, McGraw-Hill, New York, 1953.
[4] C.F. Bohren, D.R. Huffman, Absorption and Scattering of Light By Small Particles, Wiley, New York, 1998.
[5] M.O. Deville, P.F. Fischer, E.H. Mund, High-order Methods for Incompressible Fluid Flow, Cambridge University Press, Cambridge, UK, 2002.
[6] T.A. Driscoll, B. Fornber, A Padé-based algorithm for overcoming the Gibbs phenomenon, Numer. Algorithms 26 (2001) 77–92.
[8] B. Gustafsson, H. Kreiss, J. Oliger, Time Dependent Problems and Difference Methods, Wiley, New York, 1995.
[9] S.G. Johnson, J.D. Joannopoulos, Block-iterative frequency-domain methods for Maxwell's equations in a planewave basis, Opt. Express 8 (3) (2001) 173–190.

[10] Q.H. Liu, Large-scale simulations of electromagnetic and acoustic measurements using the pseudo-spectral time-domain (PSTD) algorithm, IEEE Trans. Geosci. Remote Sens. 37 (1999) 917–926.
[12] J. Gibbs, Fourier's series, Lett. Nature 59 (1898) 200.
[13] D. Gottlieb, M.Y. Hussaini, S. Orszag, Theory and applications of spectral methods, in: R.G. Voigt, D. Gottlieb, M.Y. Hussaini (Eds.), Spectral Methods for Partial Differential Equations, SIAM, Philadelphia, 1984.
[14] D. Gottlieb, S. Orszag, Numerical analysis of spectral methods: theory and applicationsCBMS-NSF Regional Conference Series in Applied Mathematics, SIAM, Philadelphia, 1977.
[15] D. Gottlieb, C.W. Shu, On the Gibbs phenomenon IV: recovering exponential accuracy in a sub-interval from a Gegenbauer partial sum of a piecewise analytic function, Math. Comput. 64 (1995) 1081–1095.
[16] D. Gottlieb, C.W. Shu, On the Gibbs phenomenon and its resolution, SIAM Rev. 30 (1997) 644–668.
[17] S. Abarbanel, D. Gottlieb, A mathematical analysis of the PML method, J. Comput. Phys. 134 (1997) 357–363.
[18] S.K. Gray, T. Kupka, Propagation of light in metallic nanowire arrays: finite-difference time domain studies of silver cylinders, Phys. Rev. B 68 (2003) 045415/1–045415/11.
[19] J.M. Oliva, S.K. Gray, Theoretical study of dielectrically coated metallic nanowires, Chem. Phys. Lett. 379 (2003) 325–331.
[21] T.W. Lee, S.C. Hagness, Pseudo-spectral time domain methods for modeling optical wave propagation in second order nonlinear materials, J. Opt. Soc. Am. B 21 (2004) 330–342.
[22] T.W. Lee, S.C. Hagness, A compact wave source condition for the pseudospectral time-domain method, IEEE Anten. Wireless Propag. Lett. 3 (2004) 253–256.
[23] S.A. Maier, P.G. Kik, H.A. Atwater, S. Meltzer, E. Harel, B.E. Kowel, A.A.G. Requicha, Local detection of electromagnetic energy transport below the diffraction limit in metal nanoparticle plasmon waveguides, Nat. Mater. 2 (2003) 229–232.
[24] M.S. Min, Spectral Method for Discontinuous Problems, Ph.D. Thesis, Brown University, 2002.
[25] M.S. Min, C.H. Teng, The instability of the Yee scheme for the "magic time step", J. Comput. Phys. 166 (2) (2001) 418–424.
[26] M.S. Min, D. Gottlieb, On the convergence of the Fourier approximation for eigenvalues and eigenfunctions of discontinuous problems, SIAM J. Numer. Anal. 40 (6) (2003) 2254–2269.
[27] M.S. Min, S.M. Kaber, W.S. Don, Fourier–Padé approximations and filtering for the spectral simulations of incompressible Boussinesq convection problem, Math. Comp. (in press).
[28] Z.S. Sacks, D.M. Kingsland, R. Lee, J.F. Lee, A perfectly matched anisotropic absorber for use as an absorbing boundary condition, IEEE Trans. Anten. Propag. 43 (12) (1995) 1460–1463.
[29] C.W. Shu, Essentially non-oscillatory and weighted essentially non-oscillatory schemes for hyperbolic conservation laws, ICASE Report No. 97-65, 1997.
[30] A. Taflove, S.C. Hagness, Computational Electrodynamics, The Finite Difference Time Domain Method, Artech House, Norwood, MA, 2000.
[31] K.S. Yee, Numerical solution of initial boundary value problems involving Maxwell's equations in isotropic media, IEEE Trans. Anten. Propag. AP-14 (1966) 302–307.